# Advection of Smooth and Non-smooth Tracers Using Spectral Bicubic Interpolation

Takeshi Enomoto(✉)

Disaster Prevention Research Institute, Kyoto University, Gokasho, Uji, Kyoto 611-0011, Japan
enomoto.takeshi.3n@kyoto-u.ac.jp
https://www.dpac.dpri.kyoto-u.ac.jp/

**Abstract.** This paper validates a semi-Lagrangian model employing the spectral bicubic interpolation scheme against a challenging suite of two-dimensional tracer advection test cases. Unlike traditional methods, the proposed scheme utilizes derivatives calculated in spectral space rather than physical space. The proposed approach is compared against three alternatives: an Eulerian model, a semi-Lagrangian model with quasi-cubic interpolation, and a non-interpolating semi-Lagrangian model.

The proposed spectral bicubic scheme consistently outperforms the alternative methods across several metrics. Advection tests using twin Gaussian hills demonstrate that the spectral bicubic scheme on a linear grid achieves the superior error convergence rate. Furthermore, the spectral bicubic scheme benefits significantly from relaxed truncation wave numbers, an advantage not observed with the quasi-cubic scheme. In simulations involving non-smooth tracer distributions, such as twin cosine bells and slotted cylinders, the spectral bicubic method exhibits fewer Gibbs ripples than the quasi-cubic approach.

The scheme also demonstrates superior mixing properties, as evidenced by the correlation between the advection of twin cosine and correlated cosine bells. While the unlimited spectral bicubic scheme does not inherently eliminate Gibbs ripples, this noise can be substantially mitigated using a quasi-monotonic short-wave filter. Finally, the model can be configured for global mass conservation with negligible computational overhead and only a minimal impact on overall accuracy.

**Keywords:** Numerical weather prediction · Tracer advection · Semi-Lagrangian method

## 1 Introduction

Advection is a fundamental process in fluid dynamics, playing a central role in the nonlinear regime. In the atmosphere, constituents such as water vapor and ozone are primary sources of the diabatic heating that drives the tropospheric

© The Author(s), under exclusive license to Springer Nature Switzerland AG 2027
O. Gervasi et al. (Eds.): ICCSA 2026 Workshops, LNCS 16760, pp. 517–533, 2027.
https://doi.org/10.1007/978-3-032-30521-3_33

and stratospheric circulation. Consequently, transport modeling remained a focal point for researchers, leading to numerous state-of-the-art transport models [6] designed to achieve desirable properties such as high accuracy, monotonicity, shape preservation [12].

The first semi-Lagrangian (SL) advection model on the sphere, which update the tracer values by interpolating at the departure points of backward-in-time trajectories, was validated against an Eulerian model using a smooth Gaussian hill in solid-body rotation over the North Pole [14]. Unlike the Eulerian model, which exhibited downstream dispersion ripples, the SL model remained stable and accurate. However, standard SL models often employ cubic interpolation, which is prone to numerical dissipation. To address this, the non-interpolating SL model (NISL) [13] reduces numerical dissipation by decomposing advection into the approximate Lagrangian component, derived from the nearest grid point, and a residual Eulerian component.

Quasi-monotonicity in numerical weather prediction (NWP) is frequently achieved using a simple limiters that restrict the interpolated values to the range of surrounding grid points [2,21]. However, this approach can induce damping by clipping the local extrema. To mitigate this, the filters may be excluded at non-monotonic intervals [19], while more sophisticated selection methods can further reduce Gibbs ripples [8,24] (See Subsect. 2.5 for details).

Because the advective-form SL scheme is not formally conservative, *a posteriori* corrections, or "fixers," are often employed to restore mass balance in NWP and climate models. This study utilizes a lightweight mass correction scheme based on a variational formulation [18], which imposes minimal changes to the solution to restore the global mass without degrading accuracy. In contrast, flux-form SL schemes [7], based on the upwind-biased finite-volume scheme [22], are inherently monotonic and formally conservative. These schemes also preserve correlations among different tracers, benefiting chemical transport models (CTMs) [16,17].

In models using the spectral transform method [9], advective terms are typically calculated in physical space. While Eulerian models benefit from accurate spectral derivatives, most SL models relinquish this advantage. To reintroduce spectral accuracy into the advective-form SL framework, the spectral bicubic interpolation (SBC) scheme was proposed [3], utilizing derivatives calculated in spectral space. Previous tests with Gaussian hill advection demonstrated that SBC outperforms traditional interpolation by simultaneously eliminating dispersion and reducing numerical dissipation. Furthermore, SBC yields global mass errors more than three order of magnitude smaller than other schemes. SBC has since been extended to a non-negative filter via arcsine transformation with Hermine cubic interpolation [4].

The purpose of this study is to validate SBC using more challenging tracer distributions in deformational flows and to evaluate its performance in both unlimited and limited cases [5]. Comparisons are made among the SL model with SBC, the Eulerian model (EUL), the SL model with the quasi-cubic interpolation (QC) scheme and non-interpolating SL model (NISL).

The remainder of the paper is organized as follows. Section 2 describes the two-dimensional advection models; Sect. 3 summarizes the test case suite; Sects. 4.1, 4.2, and 4.3 compare the unlimited models regarding convergence, overshooting, and mixing properties; Sect. 4.4 discusses the influence of quasi-monotonic filters and the global mass fixer; and Sect. 5 provides a summary and concluding discussion.

## 2 Two-Dimensional Advection Models on the Gaussian Grid

The study employs the models formulated in the previous work [3,14], updated with a two-time-level scheme [1] in place of the three-time-level scheme in the SL model. Preliminary tests with the rotation of a Gaussian hill demonstrate that the results from the two-time-level model are identical to those from the three-time-level model. Advecting winds at the midpoint are specified analytically rather than extrapolated in time to eliminate extrapolation error.

### 2.1 Governing Equation

The governing equation for two-dimensional advection of tracer $q$ on the unit sphere is

$$\frac{\mathrm{d}q}{\mathrm{d}t} = 0 \tag{1}$$

where

$$\frac{\mathrm{d}}{\mathrm{d}t} = \frac{\partial}{\partial t} + \boldsymbol{v} \cdot \nabla \tag{2}$$

is the total derivative and $\boldsymbol{v} = (u, v)$ is the wind velocity, with $u$ and $v$ representing the zonal and meridional components, respectively.

### 2.2 Eulerian Model

The Eulerian model (EUL) integrates:

$$q(t + \Delta t) = q(t - \Delta t) - \frac{2\Delta t}{\cos^2 \theta} \left( U \frac{\partial q}{\partial \lambda} + V \cos\theta \frac{\partial q}{\partial \theta} \right) \tag{3}$$

where $t$ is the present time, $\Delta t$ is the time step, $(\lambda, \theta)$ is the longitude and the latitude, and $(U, V) = (u, v) \cos\theta$ is the wind image. The variable without a time level is evaluated at $t$. All the variables and their derivatives are evaluated at the grid points without staggering. The horizontal derivatives are evaluated in spectral space.

### 2.3 Interpolating Semi-Lagrangian Model

In the interpolating SL model, the values at the next time level are predicted simply via:

$$q(\boldsymbol{g}, t + \Delta t) = q(\boldsymbol{r}, t). \tag{4}$$

In the backward trajectory scheme, the arrival point $\boldsymbol{g}$ is on the grid, while the departure point $\boldsymbol{r}$ generally is not. The trajectory is calculated along the great circle [14]. Advecting winds at $t + 1/2\Delta t$ are obtained analytically from the prescribed flow defined in Sect. 3.

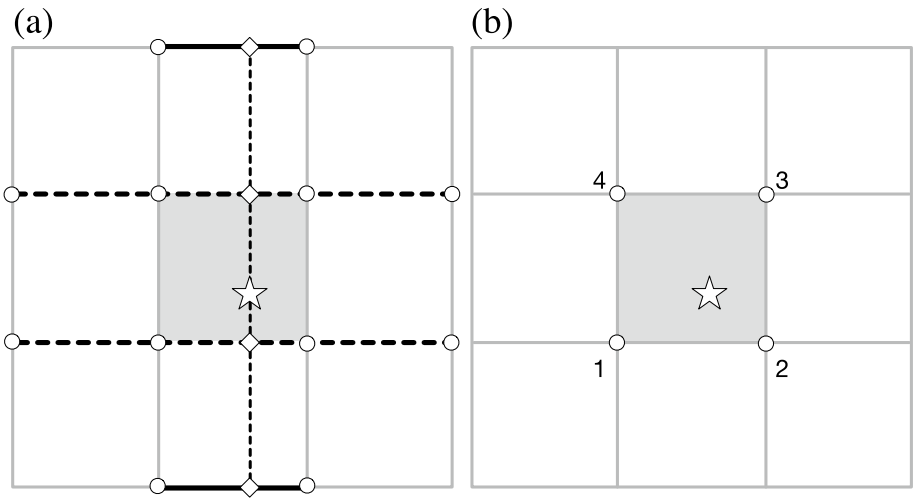


**Fig. 1.** Schematic diagrams for (a) the quasi-cubic interpolation and (b) the bicubic interpolation. The gray lines represent the model mesh. The value at the star located in the shaded stencil is found via interpolation using information on the surrounding grid points (open circles). The diamonds in panel (a) represent the temporary interpolation points at the same longitude as the interpolation point. Linear interpolation is used along the solid black lines, and the cubic Lagrange interpolation is used along the dashed black lines in panel (a). The grid-points of the stencil are labeled counter-clockwise from the bottom-left. (Color figure online)

**Quasi-Cubic Interpolation.** The QC scheme reduces the computational cost with minimal accuracy degradation compared to bicubic interpolation using the following steps [15, Fig. 1a].

1. Locate the stencil in which the target point $(\lambda, \theta)$ resides (denoted by a star).
2. Compute values at $\lambda$ with one-dimensional linear interpolation along the two latitude circles an interval away from the stencil.
3. Compute values at $\lambda$ with one-dimensional cubic Lagrange interpolation along the two latitude circles of the stencil.

4. Determine the value at $(\lambda, \theta)$ with one-dimensional cubic Lagrange interpolation along $\lambda$.

QC requires information from 12 grid points instead of 16 needed for bicubic Hermite or Lagrange interpolation.

**Spectral Bicubic Interpolation.** Bicubic interpolation is defined as

$$q = \sum_{i=1}^{4} \sum_{j=1}^{4} a_{ij} \alpha^{i-1} \beta^{j-1} \tag{5}$$

where $\alpha$ and $\beta$ are the normalized local coordinates of the target point (denoted by the star in Fig. 1b) relative to node 1:

$$\alpha = \frac{\lambda - \lambda_1}{\Delta\lambda} \tag{6}$$

$$\beta = \frac{\theta - \theta_1}{\Delta\theta} \tag{7}$$

and $(\lambda_1, \theta_1)$ is the bottom-left corner of the stencil, from which the grid points are labeled counter-clockwise, and $\Delta\lambda, \Delta\theta$ are the grid intervals. The coefficients $a_{ij}$ are determined from the values and the zonal, meridional, and cross derivatives [11]. Bicubic interpolation requires 16 values, but avoids the need for a halo when decomposed for parallel computation (Fig. 1b).

In the spectral bicubic scheme (SBC), derivatives are computed in spectral space:

$$\frac{\partial q}{\partial \lambda} = \mathrm{Re} \sum_m im q^m(\theta_j) \exp(im\lambda_i), \tag{8}$$

$$\frac{\partial q}{\partial \theta} = \mathrm{Re} \sum_m \sum_n q_n^m \exp(im\lambda_i) \frac{\mathrm{d}\tilde{P}_n^m(\theta_j)}{\mathrm{d}\theta}, \tag{9}$$

$$\frac{\partial^2 q}{\partial \lambda \partial \theta} = \mathrm{Re} \sum_m \sum_n im q_n^m \exp(im\lambda_i) \frac{\mathrm{d}\tilde{P}_n^m(\theta_j)}{\mathrm{d}\theta} \tag{10}$$

where $q^m(\theta_j)$ is the Fourier coefficient, $q_n^m$ the spherical harmonic coefficient, and $\tilde{P}_n^m(\theta_j)$ the normalized associated Legendre function. The Fourier sum in $m$ is typically computed via the Fast Fourier Transform (FFT). To save memory, the values of $\mathrm{d}\tilde{P}_n^m(\theta_j)/\mathrm{d}\theta$ are computed on the fly [20] using

$$\cos\theta_j \frac{\mathrm{d}\tilde{P}_n^m(\theta_j)}{\mathrm{d}\theta} = (n+1)\varepsilon_n^m \tilde{P}_{n-1}^m(\theta_j) - n\varepsilon_{n+1}^m \tilde{P}_{n+1}^m(\theta_j) \tag{11}$$

where

$$\varepsilon_n^m = \sqrt{\frac{n^2 - m^2}{4n^2 - 1}}. \tag{12}$$

### 2.4 Non-interpolating Semi-Lagrangian Model

The NISL model updates the values using:

$$q(\boldsymbol{g}, t + \Delta t) = q(\boldsymbol{r}^*, t - \Delta t) - 2\Delta t \boldsymbol{v}'(\boldsymbol{m}, t) \cdot \nabla q(\boldsymbol{m}, t) \tag{13}$$

where $\boldsymbol{r}^*$ is the grid point closest to the departure point, $\boldsymbol{v}' = \boldsymbol{v} - \boldsymbol{v}^*$ is the residual velocity, $\boldsymbol{v}^* = (\boldsymbol{g} - \boldsymbol{r}^*)/2\Delta t$ and $\boldsymbol{m}$ is the midpoint between $\boldsymbol{g}$ and $\boldsymbol{r}^*$ along a great circle trajectory. Interpolation is avoided for Lagrangian advection from the departure point, occurring only for the residual Eulerian advection at the midpoint. When the wind is weak enough that $\boldsymbol{g} = \boldsymbol{m} = \boldsymbol{r} = \boldsymbol{r}^*$, the model reduces to the Eulerian form (3). The phase speed error for the solid body rotation is proportional to $(m\omega'\Delta t)^2$; this is lower than the Eulerian error since $\omega' \leq \omega$ [14].

### 2.5 Shape-Preservation

Two selective filters are employed in shape-preserving cases for interpolating SL models.

The filter of SYS96 [19] suppresses the quasi-monotonic filter [2] in the interval $[x_i, x_{i+1}]$ if:

$$[f(x_i) - f(x_{i-1})][f(x_{i+2}) - f(x_{i+1})] < 0. \tag{14}$$

Then the over- and under shoots are limited by the global minimum and maximum [10].

To eliminate two-mesh Gibbs noise remaining with SYS96, the filter of [8] (NCS99) adds additional two conditions:

$$[f(x_{i-1}) - f(x_{i-2})][f(x_i) - f(x_{i-1})] > 0, \tag{15}$$

$$[f(x_{i+2}) - f(x_{i+1})][f(x_{i+3}) - f(x_{i+2})] > 0. \tag{16}$$

These constitute a five-mesh monotonicity condition. The quasi-monotonic filter is applied unless all conditions are met.

As advective-form SL models are not inherently conservative, we apply a global mass fixer SS04 [18]. Because the SBC scheme is nearly conservative [3], this variational fixer is chosen to restore mass with minimal solution perturbation.

## 3 Smooth and Non-smooth Test Cases

The standard test case suite [5] is briefly described in this section. These test cases are idealized yet modeled based on poleward advection from the tropics due to disturbances (Lauritzen, *pers. comm.*). While no analytical solution exists for the intermediate states, the initial distribution serves as the ground truth because the prescribed wind field is reversed at the midpoint of the integration period.

### 3.1 Initial Tracer Distributions

Four smooth and non-smooth distributions are defined using two centers at $\lambda_1 = 150°, \lambda_2 = 210°$ along the equator ($\theta_1 = \theta_2 = 0°$).

**Gaussian Hills.** The Gaussian hills are defined by:

$$q(\lambda, \theta) = \sum_{i=1}^{2} q_{\max} \exp\{-2b[1 - d_i]\} \tag{17}$$

where $q_{\max} = 0.95$, $b = 5$ and

$$d_i = \cos\theta \cos(\lambda - \lambda_i). \tag{18}$$

**Cosine Bells.** The cosine bells are defined by:

$$q_i(\lambda, \theta) = \begin{cases} \frac{q_{\max}}{2}[1 + \cos(\pi r_i / r_0)] & r_i < r_0 \\ 0 & r_i \geq r_0 \end{cases} \tag{19}$$

$$q(\lambda, \theta) = b + c \sum_{i=1}^{2} q_i(\lambda, \theta) \tag{20}$$

where $q_{\max} = 1$, $r_0 = 0.5$, $b = 0.1$, $c = 0.9$ and $r_i = \cos^{-1}(d_i)$.

**Slotted Cylinders.** The slotted cylinders are defined as:

$$q(\lambda, \theta) = \begin{cases} c & \text{in the following regions} \\ b & \text{otherwise} \end{cases} \tag{21}$$

where $b = 0.1$ and $c = 1$. The regions where $q = c$ are defined by $r_0 = 0.5$ and the following conditions:

- $r_i \leq r_0$, $|\lambda - \lambda_i| \geq \frac{r_0}{6}$ for $i = 1, 2$
- $r_1 \leq r_0$, $|\lambda - \lambda_1| < \frac{r_0}{6}$ and $\theta < -\frac{5}{12} r_0$,
- $r_2 \leq r_0$, $|\lambda - \lambda_2| < \frac{r_0}{6}$ and $\theta > \frac{5}{12} r_0$.

**Correlated Cosine Bells.** The correlated cosine bells are defined by:

$$q(\lambda, \theta) = \alpha q_c^2 + \beta \tag{22}$$

where $q_c$ designates the tracer distribution of the cosine bells Sect. 3.1, $\alpha = -0.8$ and $\beta = 0.9$.

### 3.2 Advecting Flows

Among the non-divergent and divergent deformational flows [5], this study focuses on the non-divergent wind field:

$$u(\lambda, \theta, t) = \frac{10}{T} \sin^2(\lambda') \sin(2\theta) \cos\left(\frac{\pi t}{T}\right) + \frac{2\pi}{T} \cos(\theta) \tag{23}$$

$$v(\lambda, \theta, t) = \frac{10}{T} \sin(2\lambda') \cos(\theta) \cos\left(\frac{\pi t}{T}\right) \tag{24}$$

where $\lambda' = \lambda - 2\pi t/T$ and $T = 5$. The time-dependent coefficient $\cos(\pi t/T)$ reverses the flow direction at $t = T/2$, returning the tracer to its initial position at $t = T$. The second term in (23) represents solid-body rotation, which translates the tracer distribution over the period $T$.

## 4 Results

Advection tests are conducted at horizontal resolutions of 3, 1.5, 0.75, 0.375 and 0.1875°. These correspond to triangular (zonal and total) truncation wave numbers T39, T79, T159, T319 and T639, respectively, on a quadratic grid, which oversamples grid points at approximately three times the truncation wave number in the zonal direction to avoid aliasing. The resolution of the interpolating SL model with QC is defined by the truncation wave number of the quadratic grid, though time integration is performed in physical space. For the interpolating SL model with SBC, simulations using a linear grid are also conducted. A linear grid uses grid points the approximately twice the truncation wave number in the zonal direction, exploiting the absence of the nonlinear advection term in the SL formulation. These simulations use truncation wave numbers of TL59, TL119, TL239, TL479 and TL959.

All of the models are integrated with Courant-Friedrichs-Lewy (CFL) number CFL = 1.0. The CFL represents the ratio of the advected distance to the grid interval; in EUL schemes, this value typically defines the threshold for numerical stability. The SL models (QC, SBC and NISL) are also tested with CFL = 5.2.

### 4.1 Convergence

We first examine model convergence on quadratic grids using smooth tracer distribution, the Gaussian hills. Figure 2 displays the convergence of the standard error norms, defined following [23], with the correspoinding convergence rates calculated via linear fit (Table 1). The norms are formulated as follows [23].

$$\ell_1 = \left[\frac{I(|q - q_t|)}{I(|q_t|)}\right], \tag{25}$$

$$\ell_2 = \left\{\frac{I[(q - q_t)^2]}{I(q_t^2)}\right\}^{1/2}, \tag{26}$$

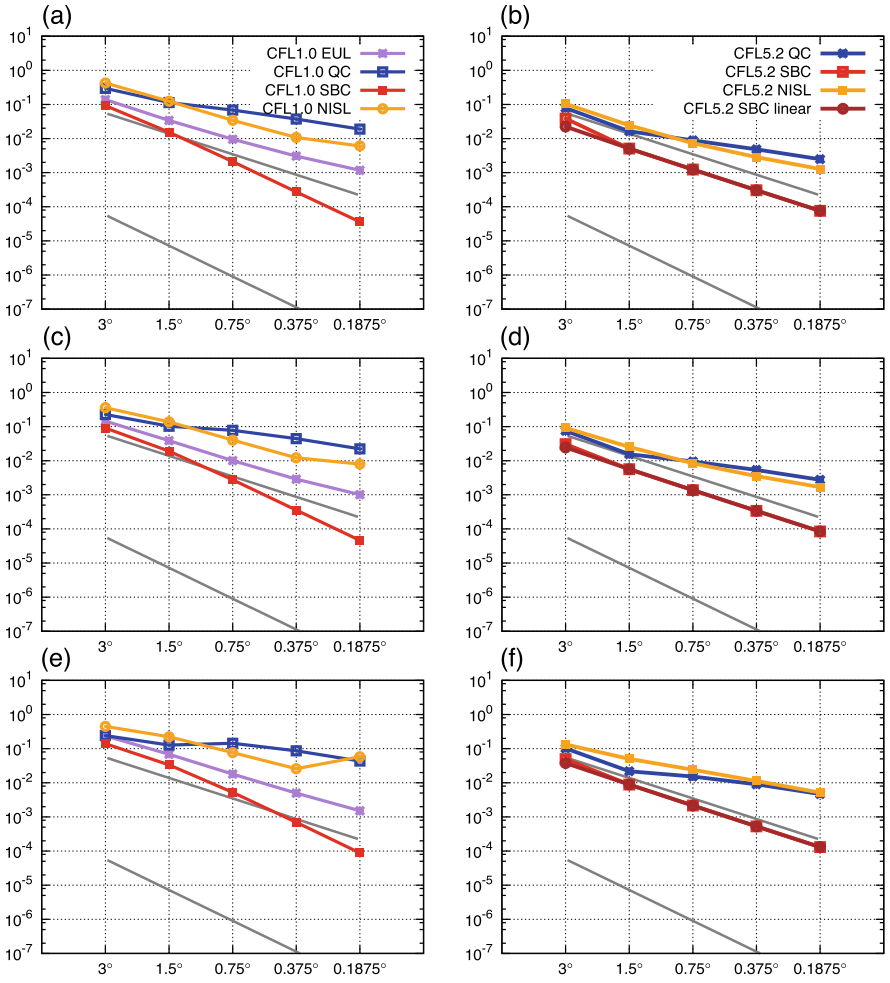


**Fig. 2.** Convergence of $\ell_1$ (a, b), $\ell_2$ (c, d) and $\ell_\infty$ (e, f) in the Eulerian model (EUL, purple), the SL models using the quasi-cubic interpolation (QC, blue) and using the spectral bicubic interpolation (SBC, red and brown for the quadratic and linear grids, respectively), and the non-interpolating SL model (NISL, orange) with the Gaussian hills for CFL = 1.0 (a, c ,e) and CFL = 5.2 (b, d, f). The upper and lower gray lines represent the second- and third-order convergences, respectively. (Color figure online)

$$\ell_\infty = \left[ \frac{\max_{\forall\lambda,\theta} |q - q_\mathrm{t}|}{\max_{\forall\lambda,\theta} |q_\mathrm{t}|} \right], \tag{27}$$

$$q_\mathrm{max} = \frac{\max_{\forall\lambda,\theta}(q) - \max_{\forall\lambda,\theta}(q_\mathrm{t})}{\Delta q_0}, \tag{28}$$

$$q_\mathrm{min} = \frac{\min_{\forall\lambda,\theta}(q) - \min_{\forall\lambda,\theta}(q_\mathrm{t})}{\Delta q_0} \tag{29}$$

where $q_t$ is the analytical value and

$$\Delta q_0 = \max_{\forall \lambda, \theta}[q(t=0)] - \min_{\forall \lambda \theta}[q(t=0)], \tag{30}$$

$$I(q) = \frac{1}{4\pi} \int_0^{2\pi} \int_{-\pi/2}^{\pi/2} q(\lambda, \theta, t) \cos\theta \mathrm{d}\lambda \mathrm{d}\theta. \tag{31}$$

EUL error norms follow a second-order convergence pattern, with rates of 1.7 for $\ell_1$ and 1.8 for $\ell_2$ and $\ell_\infty$ (Table 1). As traditional spectral models are Eulerian, these values serve as a reference.

QC and NISL exhibit degraded convergence rates. In contrast, SBC consistently outperforms the other schemes, achieving nearly third-order convergence (slopes in all norms $\approx 3.0$, Table 1) with CFL = 1.0 (Fig. 2a, c, e) and second-order convergence with CFL = 5.2 (Fig. 2b, d, f). At low resolutions the SL models (QC, SBC, and NISL) yield smaller errors with CFL = 5.2, likely due to the reduced frequency of interpolations.

Utilizing a linear grid does not improve the convergence rate for Gaussian hills; rates are identical between quadratic and linear grids for QC and SBC with CFL = 1.0. At CFL = 5.2, the SBC convergence rate using the linear grid (brown) appears slightly lower than on the quadratic grid (red). This occurs because SBC significantly reduces errors at coarse resolutions; for example, at $\Delta\lambda = 3.0$, $\ell_1, \ell_2$ and $\ell_\infty$ values for SBC are substantially improved when moving from quadratic to linear grids.

Figure 3 illustrates the equatorial cross-sections of the cosine bells for QC and SBC schemes. SBC (red) exhibits considerably less damping of the tracer amplitudes compared to QC (blue). When utilizing the linear grid, SBC (brown) retains the peaks ever more effectively. Furthermore, the numerical ripples observed between 45°E and 90°E are greatly reduced for the SBC scheme on the TL59 linear grid.

### 4.2 Non-smooth Distributions and Oscillations

Figure 4 illustrates the slotted cylinders at $t = T/2$ and $t = T$ for QC and SBC. Both schemes efficiently leverage the high resolution to maintain the tracer discontinuities. While the spatial extent of ripples in QC is limited, it exhibits significant over- and under-shooting near the cylinder edges (Fig. 5). SBC also produces oscillations, but with considerably smaller amplitudes.

Table 2 compares $\ell_2$, $q_{\max}$ and $q_{\min}$ for QC and SBC. Across all resolutions, SBC maintains a smaller $\ell_2$ norm. Notably, the absolute magnitudes of over- and under-shooting in QC increase with resolution, indicating that higher grid density exacerbates these numerical artifacts for the QC scheme.

### 4.3 Mixing Diagnostics

Mixing diagnostics evaluate the preservation of nonlinear relationship between two tracer distributions [5]. Figure 6 shows scatter plots between cosine bells

**Table 1.** Convergence rates of the Eulerian model (EUL), the interpolating SL models using quasi-cubic interpolation (QC) and using spectral bicubic interpolation (SBC) and the non-interpolating SL model (NISL) with quadratic or linear grids for the Gaussian hills.

| model | grid | CFL | $\ell_1$ | $\ell_2$ | $\ell_\infty$ |
|---|---|---|---|---|---|
| EUL | quadratic | 1.0 | 1.7 | 1.8 | 1.8 |
| QC | quadratic | 1.0 | 1.0 | 0.8 | 0.6 |
| QC | linear | 1.0 | 1.0 | 0.8 | 0.6 |
| SBC | quadratic | 1.0 | 2.8 | 2.8 | 2.7 |
| SBC | linear | 1.0 | 2.8 | 2.8 | 2.7 |
| NISL | quadratic | 1.0 | 1.6 | 1.4 | 0.9 |
| QC | quadratic | 5.2 | 1.2 | 1.1 | 1.0 |
| QC | linear | 5.2 | 1.2 | 1.1 | 1.0 |
| SBC | quadratic | 5.2 | 2.2 | 2.1 | 2.1 |
| SBC | linear | 5.2 | 2.0 | 2.0 | 2.0 |
| NISL | quadratic | 5.2 | 1.6 | 1.4 | 1.2 |

**Table 2.** Resolution dependency of $\ell_2$ for the slotted cylinders, $q_{\max}$ and $q_{\min}$ for QC and SBC for CFL = 5.2 and a quadratic grid.

| | $\ell_2$ | | $q_{\max}$ | | $q_{\min}$ | |
|---|---|---|---|---|---|---|
| $\Delta\lambda$ | QC | SBC | QC | SBC | QC | SBC |
| 3. | 0.3437 | 0.3010 | 0.1464 | 0.1710 | −0.8606 | −0.1657 |
| 1.5 | 0.2631 | 0.2180 | 0.1874 | 0.1509 | −0.1821 | −0.1353 |
| 0.75 | 0.2002 | 0.1637 | 0.1904 | 0.1721 | −0.1966 | −0.1275 |
| 0.375 | 0.1534 | 0.1218 | 0.2361 | 0.1320 | −0.2237 | −0.1036 |
| 0.1875 | 0.1195 | 0.09314 | 0.3103 | 0.1131 | −0.2842 | −0.1104 |

($\chi$) and correlated cosine bells ($\xi$) for T159 and CFL = 1.0. The curve represents the analytical relationship (22), with deviations categorized as "real" mixing ($\ell_\mathrm{r}$), unmixing ($\ell_\mathrm{u}$), or over-shooting ($\ell_\mathrm{o}$), defined following [5].

SBC has significantly smaller mixing in all norms. QC and NISL have a number of points that deviate from the curve.

SBC exhibits significantly less mixing across all norms. Conversely, QC and NISL show considerable deviations from the curve, characterized primarily by over-shooting and "real" mixing, respectively. EUL produces markedly lower unmixing and over-shooting errors than QC for CFL = 1.0.

### 4.4 Shape-Preserving Cases

Finally, we evaluate the impact of shape-preserving filters and a mass fixer. While such schemes can sometimes degrade convergence, the selective filters used here

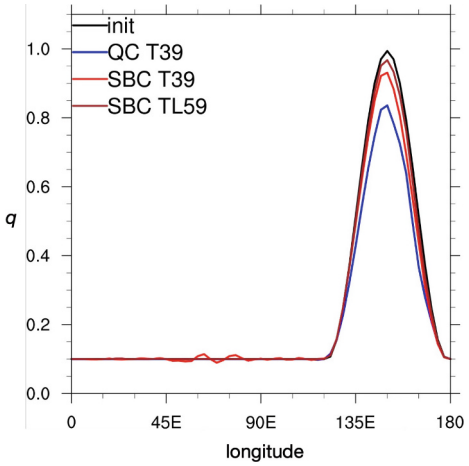


**Fig. 3.** Equatorial cross-sections of the cosine bells in longitudes between 0 and 180 at the initial time (black) at $t = T$ for QC T39 (blue), SBC T39 (red) or SBC TL59 (brown) and for CFL = 5.2. (Color figure online)

(Sect. 2.5) are designed to reduce noise while preserving local extrema. Figure 7 compares the equatorial cross-sections of the cosine bells at $t = T$ for SBC T39. The spurious ripples in the unlimited case (solid) are reduced by SYS96 (broken), but more eliminated by NCS99 (dotted). This suggests that the three-mesh condition (14) is insufficient to fully suppress high frequency Gibbs noise. The NCS99+SS04 case behaves similarly to NCS99, with only a slight reduction in peak amplitude due to the mass conservation constraint.

The shape-preserving filters effectively eliminate over- and under-shooting in the slotted cylinder test (Fig. 8). Both QC and SBC reproduce the tracer distribution well, removing artifacts near steep gradients. While QC retains the maximum value of 1.0 more effectively, SBC maintains a steeper gradient. Accuracy improves for QC in the shape-preserving case but decreases slightly for SBC (Table 3). Consequently, while both schemes perform similarly under these constraints, SBC retains marginal advantage across all resolutions.

## 5 Concluding Remarks

A two-dimensional advection model using the SL scheme with SBC has been compared against EUL, the SL model with QC and NISL in a suite of test cases [5]. In the convergence tests using twin Gaussian hills, SBC is found to produce the smallest errors and the best error-convergence rate. Furthermore, SBC benefits from the use of a linear grid with a larger truncation wave number for the same number of grid points, whereas QC does not. Cross-sections of the cosine bells and slotted cylinders show that the amplitudes of the over- and under- shooting in QC are large near the tracer boundaries, even if their spatial

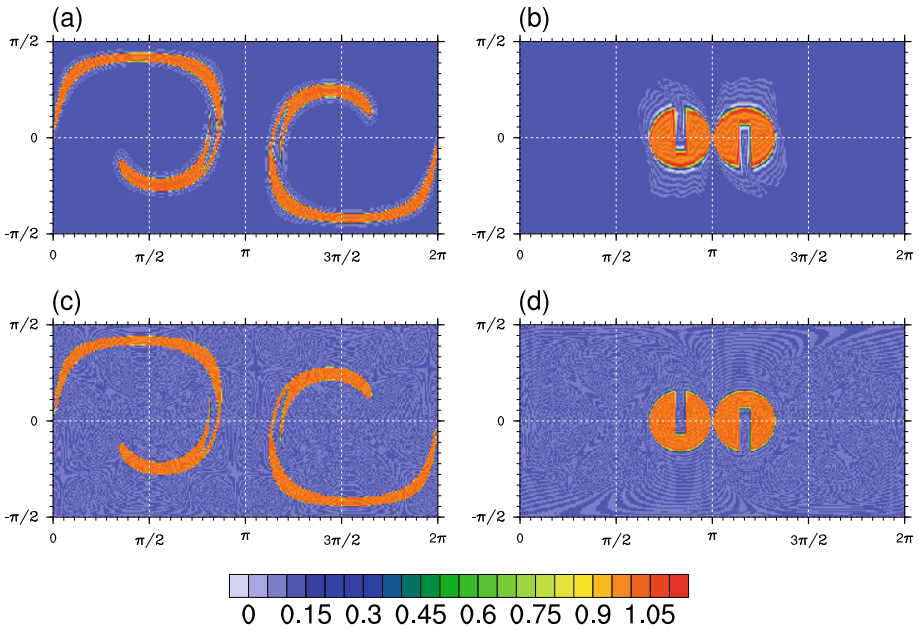


**Fig. 4.** Tracer distributions for QC (a, b) and SBC (c, d) with the slotted cylinders at $t = T/2$ (a, c) and $t = T$ (b, d) for CFL = 5.2 and for T639.

**Table 3.** Same as Table 2 but using the short-wave filter [8] and the global mass correction [18].

| | $\ell_2$ | | $q_{\max}$ | | $q_{\min}$ | |
|---|---|---|---|---|---|---|
| $\Delta\lambda$ | QC | SBC | QC | SBC | QC | SBC |
| 3. | 0.3623 | 0.3363 | 0. | 0. | 0. | 0. |
| 1.5 | 0.2794 | 0.2493 | 0. | 0. | 0. | 0. |
| 0.75 | 0.2120 | 0.1882 | 0. | 0. | 0. | 0. |
| 0.375 | 0.1612 | 0.1397 | 0. | 0. | 0. | 0. |
| 0.1875 | 0.1211 | 0.1048 | 0. | 0. | 0. | 0. |

extent is limited. While SBC produces over- and under-shooting that spreads more extensively, the amplitudes are smaller than those of QC.

Mixing diagnostics show the advantages of SBC; its mixing norms are smaller than those of alternative methods, and it benefits from relaxed truncation, particularly at coarse resolutions. Notably, over-shooting and "real" mixing are prominent in QC and NISL, respectively.

The computational tests demonstrate that SBC outperforms EUL, QC and NISL. SBC yields smaller error norms with ideal convergence and reduced over- and under-shooting, which can be further controlled using a selective filter and

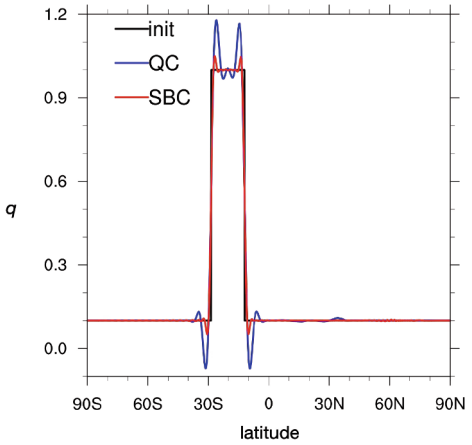


**Fig. 5.** Meridional cross-sections of $q$ at 150°E at $t = 0$ (black) and at $t = T$ for QC (blue) and SBC (red) for T639 and for CFL = 5.2. (Color figure online)

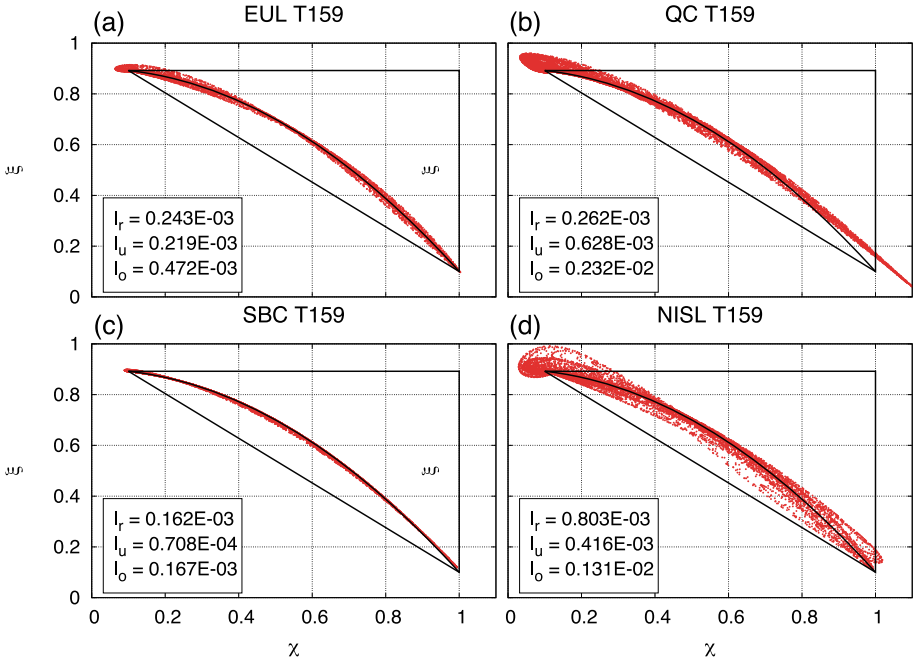


**Fig. 6.** Scatter plots displaying the relationship between the cosine bells and the correlated cosine bells for (a) EUL, (b) QC, (c) SBC and (d) NISL for CFL = 1.0 and T159 at $t = T/2$.

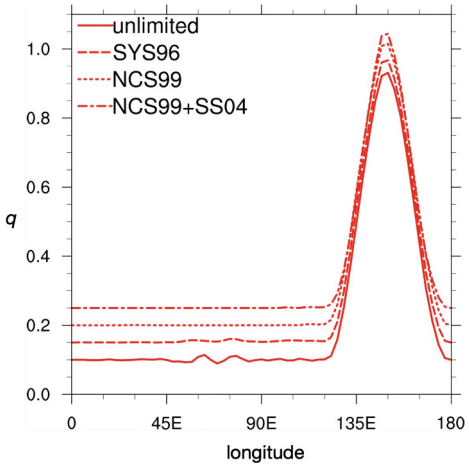


**Fig. 7.** Same as Fig. 3 with SBC T39 but using the short-wave filters and the global mass correction. Note that SYS96 (broken), NCS99 (dotted) and NCS99+SS04 (dash-dotted) are shifted upward by 0.05, 0.1 and 0.15, respectively, for clarity.

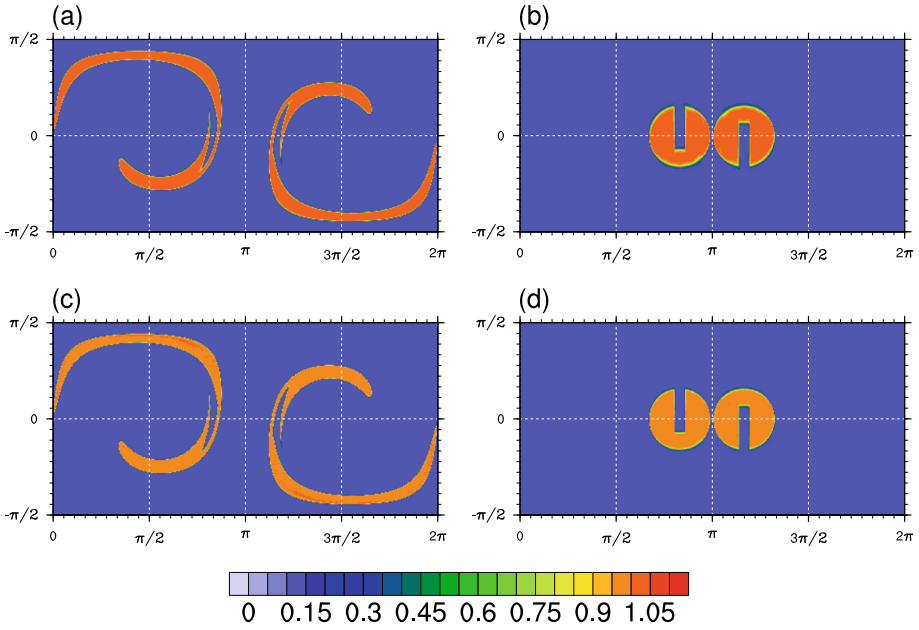


**Fig. 8.** Same as Fig. 4 but using NCS99 and SS04.

excellent mixing properties. While SBC requires an additional inverse Legendre transform to obtain meridional derivatives, the heuristic computational gain is substantial. Because SBC achieves comparable accuracy to QC at half the trun-

cation wave number, the total number of grid points is reduced by a factor of four. Furthermore, since the complexity of the spectral transforms scales with the cube of the truncation wave number, the saving from operating at a coarser resolution significantly outweigh the overhead of the additional transform.

A somewhat unexpected finding is that the EUL can be more accurate than QC or NISL in mixing diagnostics. While SL advection schemes are often chosen over the Eulerian methods to avoid unrealistic ripples, these mixing diagnostics show that this is not always the case. However, if a larger time step (fewer interpolations) or a more accurate interpolation schem like SBC is used, SL mixing diagnostics improve significantly, outperforming EUL even for CFL = 1.0. These results underscore the importance of numerical accuracy alongside properties typically prioritized in tracer advection, such as conservation or monotonicity.

**Acknowledgement.** This work was supported by JSPS KAKENHI Grant Number 15K13417, 21K03662, and 24H00021. The code is available from https://github.com/tenomoto/advection. The NCAR Command Language 6.3.0 (UCAR, 2015) and gnuplot 5.0 scripts provided by Dr Lauritzen were used for analysis and visualization with modification. The author thanks three anonymous reviewers for constructive comments.

**Disclosure of Interests.** The author does not have any competing interests.

## References

1. Bates, J.R., McDonald, A.: Multiply-upstream, semi-Lagrangian advective scheme: analysis and application to a multi-level primitive equation model. Mon. Wea. Rev. **110**(12), 1831–1842 (1982). https://doi.org/10.1175/1520-0493(1982)110⟨1831:MUSLAS⟩2.0.CO;2
2. Bermejo, R., Staniforth, A.: The conversion of semi-Lagrangian advection schemes to quasi-monotone schemes. Mon. Wea. Rev., **120**(11), 2622–2632 (1992). https://doi.org/10.1175/1520-0493(1992)120⟨2622:TCOSLA⟩2.0.CO;2
3. Enomoto, T.: Bicubic interpolation with spectral derivatives. SOLA **4**, 5–8 (2008). https://doi.org/10.2151/sola.2008-002
4. Kashimura, H., Enomoto, T., Takahashi, Y.O.: Non-negative filter using arcsine transformation for tracer advection with semi-Lagrangian scheme. SOLA **9**, 125–128 (2013) https://doi.org/10.2151/sola.2013-028
5. Lauritzen, P.H., Skamarock, W.C., Prather, M.J., Taylor, M.A.: A standard test case suite for two-dimensional linear transport on the sphere. Geosci. Model Dev. **5**(3), 887–901 (2012). https://doi.org/10.5194/gmd-5-887-2012
6. Lauritzen, P.H., Coauthors: A standard test case suite for two-dimensional linear transport on the sphere: results from a collection of state-of-art schemes. Geosci. Model Dev., **7**(1), 105–145 (2014). https://doi.org/10.5194/gmd-7-105-2014
7. Lin, S.-J., Rood, R.B.: Multidimensional flux-form semi-Lagrangian transport schemes. Mon. Wea. Rev. **124**(9), 2046–2070 (1996). https://doi.org/10.1175/1520-0493(1996)124⟨2046:MFFSLT⟩2.0.CO;2
8. Nair, R., J. Côté, Staniforth, A.: Monotonic cascade interpolation for semi-Lagrangian advection. Quart. J. Roy. Meteor. Soc. **125**(553), 197–212 (1999). https://doi.org/10.1002/qj.49712555311

9. Orszag, S.A.: Transform method for the calculation of vector-coupled sums: application ot the spectral form of the vorticity equation. J. Atmos. Sci. **27**(6), 890–895 (1970). https://doi.org/10.1175/1520-0469(1970)027⟨0890:TMFTCO⟩2.0.CO;2
10. Ostiguy, L., Laprise, J.P.R.: On the positivity of mass in commonly used numerical transport schemes. Atmos.–Ocean, **28**(2), 147–161 (1990). https://doi.org/10.1080/07055900.1990.9649371
11. Press, W.H., Flannery, B.P., Teukolsky, S.A., Vetterling, W.T.: Numerical recipes in Pascal. Cambridge University Press, Cambridge, UK (1989)
12. Rasch, P.J., Williamson, D.L.: Computational aspects of moisture transport in global models of the atmosphere. Quart. J. Roy. Meteor. Soc. **116**(495), 1071–1090 (1990). https://doi.org/10.1002/qj.49711649504
13. Ritchie, H.: Eliminating the interpolation associated with the semi-Lagrangian scheme. Mon. Wea. Rev. **114**(1), 135–146 (1986). https://doi.org/10.1175/1520-0493(1986)114⟨0135:ETIAWT⟩2.0.CO;2
14. Ritchie, H.: Semi-Lagrangian advection on a Gaussian grid. Mon. Wea. Rev. **115**(2), 608–619 (1987). https://doi.org/10.1175/1520-0493(1987)115⟨0608:SLAOAG⟩2.0.CO;2
15. Ritchie, H., Temperton, C., Simmons, A., Hortal, M. Davies, T., Dent D., Hamrud, M.: Implementation of the semi-Lagrangian method in a high-resolution version of the ECMWF forecast model. Mon. Wea. Rev. **123**(2), 489–514 (1995). https://doi.org/10.1175/1520-0493(1995)123⟨0489:IOTSLM⟩2.0.CO;2
16. Štajner, I., Riishøjgarrd, L.P., Rood, R.B.: The GEOS ozone data assimilation system: specification of error statistics. Quart. J. Roy. Meteor. Soc. **127**(573), 1069–1094 (2001). https://doi.org/10.1002/qj.49712757320
17. Sudo, K., Takahashi, M. Kurokawa, J. and Akimoto, H.: CHASER: a global chemical model of the troposphere 1. model description. J. Geophys. Res. **107**(4339), ACH 7-1–ACH 7–20 (2002). https://doi.org/10.1029/2001JD001113
18. Sun, W.-Y., Sun, M.-T.: Mass correction applied to semi-Lagrangian advection scheme. Mon. Wea. Rev. **132**(4), 975–984 (2004). https://doi.org/10.1175/1520-0493(2004)132⟨0975:MCATSA⟩2.0.CO;2
19. Sun, W.-Y., Yeh, K.-S., Sun, R.-Y.: A simple semi-Lagrangian scheme for advection equation. Quart. J. Roy. Meteor. Soc. **122**(533), 1211–1226 (1996). https://doi.org/10.1002/qj.49712253310
20. Temperton, C.: On scalar and vector transform methods for global spectral models. Mon. Wea. Rev. **119**(5), 1303–1307 (1991). https://doi.org/10.1175/1520-0493-119-5-1303.1
21. Temperton, C., Hortal, M., Simmons, A.: A two-time-level semi-Lagrangian global spectral model. Quart. J. Roy. Meteor. Soc. **127**(571), 111–127 (2001). https://doi.org/10.1002/qj.49712757107
22. van Leer, B.: Towards the ultimate conservative difference scheme. ii. Monotonicity and conservation combined in a second-order scheme. J. Comp. Phys. **14**(4), 361–370 (1974). https://doi.org/10.1016/0021-9991(74)90019-9
23. Williamson, D.L., Drake, J.B., Hack, J.J., Jakob, R., Swarztrauber, P.N.: A standard test set for numerical approximations to the shallow water equations in spherical geometry. J. Comp. Phys. **102**(1), 211–224 (1992). https://doi.org/10.1016/S0021-9991(05)80016-6
24. Zerroukat, M., Wood, N., Staniforth, A.: A monotonic and positive-definite filter for a semi-Lagrangian inherently conserving and efficient (slice) scheme. Quart. J. Roy. Meteor. Soc. **131**(611), 2923–2936 (2005). https://doi.org/10.1256/qj.04.97